Dry Coupled Ultrasonic Non-Destructive Evaluation using an Over-Actuated Unmanned Aerial Vehicle

Robert Watson*, Mina Kamel, Dayi Zhang, *Member, IEEE*, Gordon Dobie, Charles MacLeod, S. Gareth Piece and Juan Nieto, *Member, IEEE*

***Abstract*—Unmanned Aerial Vehicles (UAVs) are seeing increasing adoption to automated remote and in situ inspection of industrial assets, removing the need for hazardous manned access. Aerial manipulator architectures supporting pose-decoupled exertion of force and torque would further enable UAV deployment of contact-based transducers for sub-surface structural health assessment. Herein, for the first time, we introduce an over-actuated multirotor deploying a dry-coupled ultrasonic wheel probe as a novel means of wall thickness mapping. Using bi-axial tilting propellers in a unique tricopter layout, this system performs direct thrust vectoring for efficient omnidirectional flight and application of interaction forces. In laboratory testing we demonstrate stable and repeatable probe deployment in a variety of representative asset inspection operations. We obtain a mean absolute error in measured thickness of under 0.10 mm when measuring an aluminum sample with varying wall thickness. This is maintained over repeated exit and re-entry of surface contact, and when the sample is mounted vertically or on the underside of a 45° overhang. Furthermore, when rolling the probe dynamically across the sample surface in an area scanning modality, a mean absolute error in wall thickness below 0.28 mm is recorded. Multi-modal operational confidence bounds of the system are thereby quantitatively defined.**

***Note to Practitioners*—Motivation for this paper stems from the desire to enhance the speed and level of insight into structural health currently offered through remote aerial inspection processes. We approach this by integration of a thrust vectoring multirotor platform with a dry-coupling wheel probe for aerial ultrasonic thickness measurement. This system reliably presses the probe into the target surface and obtains point measurements across various surface orientations without a stabilizing frame. This broadens applicability and permits novel inspections where couplant gel would otherwise contaminate the surface and require manual cleaning. We profile thickness along a scanned linear section, a mode suited to corrosion mapping of large surface areas such as petrochemical storage tanks, pipework or similar assets. We also make detailed consideration towards measurement accuracy, repeatability and localization, an aspect commonly overlooked in literature. Future work to characterize variable friction effects currently limiting rolling scan speed and measurement coverage density may be beneficial. Quantitative study of the impact to dry-couplant effectiveness of any uncommon surface contamination specific to a desired application is also advised.**

***Index Terms*—Unmanned Aerial Vehicles, Inspection, Ultrasound, Dry-Coupling, Wheel-Probe, Over-Actuation**

I. Introduction

INDUSTRIAL inspection is a time consuming and laborious process often taking place in environments hazardous for human technicians. In situ assessment of industrial assets is required under law to ascertain sufficient evidence of their continued fitness for safe and efficient operation [1], [2]. Resultant data are then used to inform operation decisions and preventative maintenance strategies. To fully profile their health status and degradation over time, assets require frequent inspections, increasing in regularity as they age past their design life [3]. Energy sector infrastructure is a key example. Lost revenue during shutdown for inspection can become an increasingly significant expense for asset operators, exacerbated by lengthy procedures to ensure inspector safety.

Automated Non-Destructive Evaluation (NDE) procedures are therefore of great interest. Amid “Industry 4.0” discussions, automation offers increased inspection speed, more traceable, quantitative profiles of asset health, and is less subjective to inspector opinion or fatigue [4], [5]. Under this drive, multirotor Unmanned Aerial Vehicle (UAV) systems have become well established as an initial, non-contact, visual screening tool across the energy and civil engineering sectors. Surveyed assets include: solar panels [6], power lines [7], wind turbines [8], bridges [9] and quarries [10]. Recent advancements involve photogrammetric reconstruction [11] for extended timescale monitoring, and machine vision assisted defect identification to reduce analysis times [12].

However, these non-contact, visual methods grant little insight below the asset outer surface. To better determine structural health, inspection must draw upon volumetric NDE methods such as ultrasonic testing [13].

In ultrasonic inspection, a pressure wave-packet is transmitted into the object under test and reflected by acoustic discontinuities: defect features or component boundaries. Time-domain analysis of the returned ultrasonic waveform signal permits feature localization for volumetric structural assessment. Commonly, water-based gel couplant displaces the highly reflective air layer between the probe and target material, better matching their acoustic impedances and enabling ultrasonic wave transmission.

By contrast, dry-coupling strategies use pressure applied to a deformable material at the probe-target interface to

mechanically expunge the air layer. Their usage is established in conventional inspections when liquid couplant would contaminate or weaken target structures [14], water bath immersion is inappropriate, or subsequent cleanup operations are impractical [15], [16]. Advancements in material science see their extension to dry-coupling, solid core, wheel probes [17], smaller and lighter than fluid core designs.

Within the context of aerial NDE, operation without an onboard gel reservoir will reduce payload and extend flight times, also eliminating center of mass variation when dispensing gel. Further, there is no need to continually replenish a gel supply during extended area scanning.

Multiple potential applications for aerial ultrasonic thickness measurement are apparent to corrosion monitoring in the presence of restricted manned access, particularly across the energy sector. Large areas of petrochemical storage tank walls can be corroded by their contents [18]. Their decontamination of caustic liquids for manned NDE may entail downtime upwards of 100 days [19]. Within power generation and chemical processing plants, pipe networks with limited accessibility are subject to destructive effects such as flow accelerated corrosion [20]. Monitoring corrosion in steel chimney stacks [21] and regions of offshore oil and gas platforms above the waterline [22] can entail hazardous roped access. Similarly, hydrogen sulfide gas buildup can pose hazards to manned internal corrosion monitoring above the waterline in the monopile of offshore wind platforms [23].

However, the controlled physical interaction required for contact-based ultrasonic NDE in such scenarios, represents a challenge for conventional multirotor platforms, as illustrated in Fig. 1. The common unidirectional thrust multirotor must reorientate the entire aircraft to exert force or reject external disturbances. Doing so moves the probe relative to the surface, impacting sensor coupling and measurement quality. For stability, commercial systems using this configuration rely on large outriggers or magnetic adhesion, increasing payload and degrading maneuverability [24]–[26].

Strategies to improve UAV efficacy as aerial workers include embedding robotic manipulators aboard the craft or thruster layout reconfiguration, improving dynamic capability without significant additional hardware. In the latter case, the platform itself becomes fully or over-actuated and is able to generate force and torque in 6 Degrees of Freedom (DoF), without altering its pose. This effect may be achieved via a number of fixed orientation propellers, with thrust acting in superposition to generate desired net force at the cost of efficiency [27], or by actively re-orienting thrusters when force generation is desired, retaining the more efficient unidirectional layout in free flight [28]. Such architectures can reject disturbance while holding a sensor in stationary contact.

A. Related Works

To date a limited selection of works have directly recognized this utility of aerial robotic platforms to perform contact-based in situ NDE. Most prominently, the AeroX octocopter uses multidirectional thrust superposition and a gel-coupled, dual-element, ultrasonic probe mounted at the end of a 6 DoF actuated manipulator arm to inspect oil refinery storage tanks and pipe sections [29]. The large 1.7 m by 2.3 m UAV with a maximum take-off weight of 25 kg captured thickness measurement to the satisfaction of an NDE inspector but no quantitative claim is made to its accuracy.

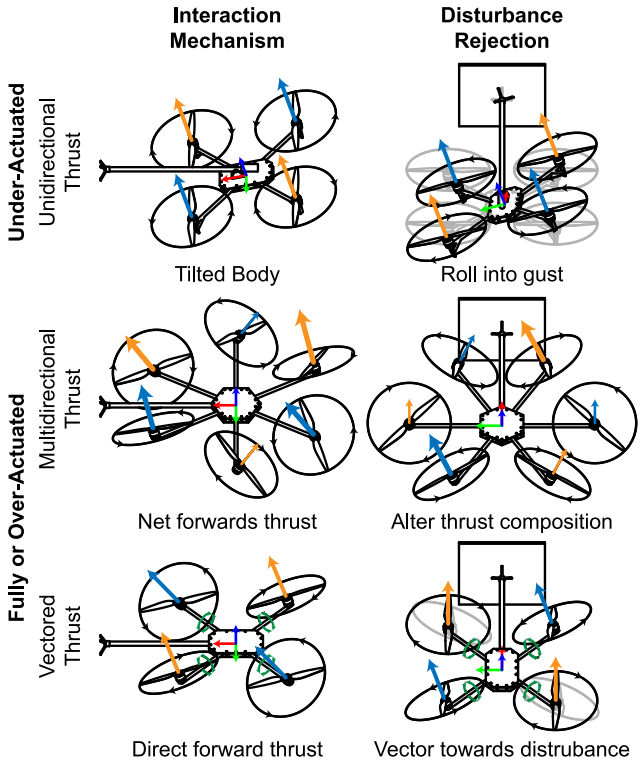

Fig. 1. A comparison of multirotor configurations for environmental interaction. Propeller relative thrust is indicated by arrow size. The illustrated disturbance response corresponds to rejection of a gust of wind from the left of the image. Undisturbed craft position is shown in grey.

Tognon *et al* present an alternate configuration in the OTHex multidirectional-thrust hexacopter, using a 2 DoF manipulator arm to successfully localize weld material on a horizontal pipe section with an eddy current probe [30]. They make no comment regarding assessment of weld integrity. Sanchez-Cuevas *et al* use a similar fully-actuated hexacopter to access the underside of a concrete bridge, maintaining contact using an outrigger frame atop the UAV, but present no structural NDE data [31]. Building on previous work [32], using a hexacopter layout with 12 vectored propellers Bodie *et al* [33], [34] generate 6 DoF pose-decoupled force and torque. They inspect a reinforced concrete block at 5 cm intervals using a half cell potential mapping circuit grounded to the sample.

Other strategies bypassing the problems of under-actuation have also proven somewhat successful. Jarvis *et al* use a quadcopter to land a discrete Electro-Magnetic Acoustic Transducer (EMAT) sensor package atop a horizonal steel sheet and pipe section with success rates of 65% and 60%, respectively [35]. Ultrasonic measurement of a vertical metal plate is conducted in [36] using a large supporting outrigger to maintain contact. Updates to this system [37] apply horizontal thrust into the plate via two additional propellers, but do not grant full-actuation. Kocer et al demonstrate a proof of concept

controller for ultrasonic thickness measurement of the underside of a horizontal acrylic plate using a standard quadcopter [38]. Others conduct ultrasonic measurement via short-duration contact with a vertical plate under autonomous control from a planar lidar sensor [39].

More novel strategies involve using a 1 DoF manipulator to perform a "tap-test" for voids in concrete bridge material [40] or to place and retrieve an embedded structural health monitoring sensor [41]. Further application agnostic review of aerial interaction strategies may be found in [42].

B. Problem Statement

Aerial contact-based NDE of industrial assets is a nascent research direction, evolving rapidly in recent years with the goal of remote sub-surface structure assessment. Existing literature shows significant development of supporting multirotor platforms, but can overlook the quality of gathered data and their utility towards meaningful automated inspection. Methods employing under-actuated systems in particular are often limited in positioning accuracy and repeatability. Multidirectional thrust architectures are inefficient, persistently counteracting unwanted thrust components. Hence, in addition to developing novel aerial inspection platforms and methodologies, demonstration of accurate and reliable measurement providing known confidence bounds is essential for industrial technology adoption.

C. Contributions to Knowledge

In response to the challenges facing aerial contact-based ultrasonic NDE, we develop a novel means for automation of the in situ inspection of industrial assets. In particular, this paper presents the following contributions:

- A novel aerial inspection system incorporating dual-axis tilting propellers in a tricopter architecture for environmental interaction via dynamic thrust vectoring.
- A modified hybrid position-force controller for omnidirectional aerial interaction and deployment of contact based deformable ultrasonic probes.
- Stable and repeatable multidirectional aerial ultrasonic thickness point measurement without an embedded robotic arm or supporting frame.
- A new mode of aerial ultrasonic inspection for scenarios not suited to couplant gel via a dry-coupled wheel probe.
- Coupling force adaptive ultrasonic signal processing and cross-sectional thickness visualization algorithms for presentation of UAV acquired dynamic scan data.
- A detailed and application focused quantification of the multi-modal aerial ultrasonic NDE positioning and measurement accuracy confidence bounds.

D. Manuscript Structure

The remainder of this paper is constructed as follows. Through Section II we provide an overview of the integrated UAV inspection system and operating principles. In Section III the experimental methodology used to demonstrate and assess system capability is described. Section IV provides an analysis of the results of this study, accompanied by further discussion in Section V. Objectives for future work are given in Section VI. Finally, conclusions drawn from this article are provided in Section VII.

II. System Overview

A. Voliro Tri-Copter

Here, we describe the Voliro Tricopter, an aerial platform specifically designed for remote airborne physical interaction.

1) Aerial Platform Hardware

The aerial robot used in this paper is an omnidirectional multirotor capable of generating 6 DoF wrench. The UAV is composed of two main thrusters capable of thrust vectoring by turning around 2 axes, and a tail thruster capable of inverting the force direction as shown in Fig. 2.

Ability to safely maintain surface contact is an important consideration during aerial inspection. As such, the Voliro Tricopter is rated for flight in windspeeds up to 12 m/s. Optional rotor guards may be attached, protruding beyond the rotor swept volume in the body x-axis. These protect the target from rotor collision during severe disturbances and are employed during our empirical assessments. Further, the 6 DoF wrench exertion capability enables the UAV to enter a configuration well suited to physical interaction, wherein external disturbances may be directly opposed while maintaining static and reliable sensor placement. The Voliro Tricopter can exert up to 30 N net force in all directions in addition to supporting the total system mass of 4 kg.

It is equipped with a Pixhawk flight controller for state estimation and low level flight control. An intel NUC i7 core computer running the Robot Operating System (ROS) is embedded within the UAV to enable autonomous features and data recording. Communication between the NUC computer and Pixhawk flight controller is enabled via a serial data port.

This network supports data from various onboard and offboard position estimation technologies for both indoor and outdoor deployment. In addition to common Global Navigation Satellite Systems (GNSS), examples include ground based optical motion capture systems (such as Vicon [43]), laser tracking via reflective prism [44], and visual odometry [45]. The most appropriate positioning technology may be selected based on its operating characteristics and the intended use case.

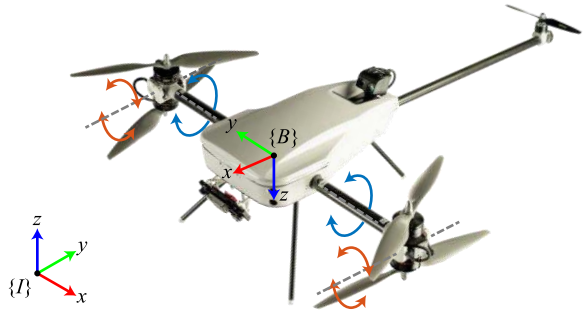

Fig. 2. The Voliro tricopter aerial manipulation platform. Annotations show the body and inertial world coordinate frames and axes of actuation granting 6 DoF wrench exertion. Both propeller arms rotate independently. Bi-propeller assemblies rotate in one further axis about the tip of these arms.

2) Control Structure

In this section, we describe the baseline controller for the Voliro tricopter platform, used to autonomously maintain inflight pose and generate interaction force as set by the pilot. This is similar to the architecture described in [32], so is presented in summary for system context alongside modifications in support of environmental interaction using the bi-axial tilting propeller tricopter platform. Fig. 3 gives a diagram of the controller structure, leveraging the decoupling of position and attitude dynamics intrinsic to an omni-directional platform.

We use two coordinate frames to describe the controller function: the inertial world frame $\{I\}$ and the UAV affixed body frame $\{B\}$, as in Fig. 2. Bold typeface indicates a vector parameter unless otherwise stated. We denote the reference frame of a parameter using left-hand superscript. An estimate of parameter $\boldsymbol{x}$ is denoted with the hat symbol as $\hat{\boldsymbol{x}}$, where its desired value is $\boldsymbol{x}_{des}$ and its time derivative is $\dot{\boldsymbol{x}}$. The rotation matrix expressing orientation of $\{B\}$ relative to $\{I\}$ is denoted ${}^{I}_{B}\boldsymbol{R}$ with transpose ${}^{I}_{B}\boldsymbol{R}^{T}$, whereas the quaternion expression is ${}^{I}_{B}\boldsymbol{q}$ with complex conjugate ${}^{I}_{B}\boldsymbol{q}^{*}$.

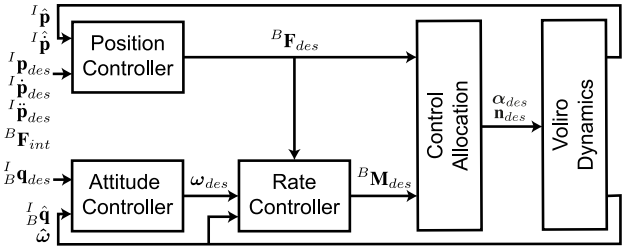

Fig. 3. A block diagram of the Voliro control structure used to maintain omnidirectional stability and perform environmental interaction.

The position controller forms the outermost loop. This generates desired force commands, ${}^{B}\boldsymbol{F}_{des}$, based on a PID evaluation of position error in $\{I\}$, ${}^{I}\boldsymbol{p}_{err}$. Additional components balance UAV weight, $m\boldsymbol{g}$, and feedforward force for the desired acceleration, ${}^{I}\ddot{\boldsymbol{p}}_{des}$. The PID controller constants are k_p, k_i, k_d. The result is expressed in $\{B\}$ via rotation. Desired interaction force is included as ${}^{B}\boldsymbol{F}_{int}$, a vector aligned with the x-axis of $\{B\}$ having zero magnitude during free flight.

$$ {}^{I}\boldsymbol{p}_{err} = {}^{I}\boldsymbol{p}_{des} - {}^{I}\hat{\boldsymbol{p}} \tag{1} $$

$$ {}^{B}\boldsymbol{F}_{des} = {}^{I}_{B}\boldsymbol{R}^{T}\left(k_p\,{}^{I}\boldsymbol{p}_{err} + k_i\int {}^{I}\boldsymbol{p}_{err}\,dt + k_d\,{}^{I}\dot{\boldsymbol{p}}_{err} + m\boldsymbol{g} + m\,{}^{I}\ddot{\boldsymbol{p}}_{des}\right) + {}^{B}\boldsymbol{F}_{int} \tag{2} $$

When interaction is requested, the controller transitions to a flight-mode in support of force application. While maintaining position in the other axes, ${}^{B}\boldsymbol{F}_{des}$ in the $\{B\}$ x-axis is then set by ${}^{B}\boldsymbol{F}_{int}$ at a magnitude meeting the specific requirements for deployment of the contact-based NDE sensor. Known platform geometry and propeller thrust characteristics enable open-loop force and torque generation with sufficient accuracy to meet application demands. This control block thereby serves as a hybrid force-position controller.

The attitude controller consists of two cascaded blocks. The first computes the desired body rotation rate, $\boldsymbol{\omega}_{des}$, in proportion to the quaternion orientation error, $\boldsymbol{q}_{err}$, via control parameter k_q. This error is computed via quaternion product, and is expressed in scalar-vector component form. The vector component, $\boldsymbol{q}_{v,err}$, dictates the body rate direction and magnitude whereas the sign of the scalar component, $q_{w,err}$, avoids the unwinding phenomenon, caused by the dual representation of orientations in quaternion space.

$$ \boldsymbol{q}_{err} = {}^{I}_{B}\boldsymbol{q}_{des} \otimes {}^{I}_{B}\hat{\boldsymbol{q}}^{*} = \begin{pmatrix} q_{w,err} \\ \boldsymbol{q}_{v,err} \end{pmatrix} \tag{3} $$

$$ \boldsymbol{\omega}_{des} = k_q\, sgn\left(q_{w,err}\right)\boldsymbol{q}_{v,err} \tag{4} $$

The second attitude block then gives the desired body moments, ${}^{B}\boldsymbol{M}_{des}$. These are proportional to the body rate error by constant k_r, also compensating for the UAV inertia, $\boldsymbol{J}$, and the moment due to the net thrust and center of mass offset from the origin of $\{B\}$, ${}^{B}\boldsymbol{r}_{off}$.

$$ {}^{B}\boldsymbol{M}_{des} = k_r(\boldsymbol{\omega}_{des} - \hat{\boldsymbol{\omega}}) - {}^{B}\boldsymbol{r}_{off} \times {}^{B}\boldsymbol{F}_{des} + \hat{\boldsymbol{\omega}} \times \boldsymbol{J}\hat{\boldsymbol{\omega}} \tag{5} $$

Finally, in the control allocation stage, desired arm angles, $\boldsymbol{\alpha}_{des}$, and rotor speeds, $\boldsymbol{n}_{des}$, minimizing total thrust are quickly calculated from the desired force and moment vector by Moore-Penrose pseudo-inverse of the static system matrix and trigonometric identity [29], [32], [33]. These command signals are then distributed to the arm actuation servos and propeller motor speed controllers.

B. Contact NDE Payload

The hardware that comprises the inspection payload consists of two main components: a dry-coupling wheel probe and a custom designed transceiver circuit board, both mounted aboard the UAV manipulator platform.

1) Dry-Coupling Wheel Probe

The wheel probe houses two piezoelectric ultrasonic elements with nominal center frequency of 5 MHz [46]. These are embedded within an axial shaft, as depicted in the cross-sectional view of Fig. 4. Surrounding the axle is a freely rotating, deformable, rubberized tire providing minimal attenuation of the ultrasonic signal during propagation between the piezoelectric element and sample material.

The most appropriate ultrasonic probe for a given inspection scenario varies with the defect feature of interest and target object. A twin-element transducer, such as this, may be well suited to remaining wall thickness measurements of corroded samples per current ISO [47] and ASTM [48] standards. The angled wave propagation path increases sensitivity to echoes from the base of corrosive pits, useful for minimum wall thickness measurement. Further, dedicated transmit and receive elements prevent masking of the returning signal during the brief relaxation period of a piezoelectric transducer immediately following transmission; a common occurrence in thin samples. An internal acoustic barrier bisecting the tire

prevents direct cross-talk between elements and ensures the receiver is able to capture signals at the instant of transmission.

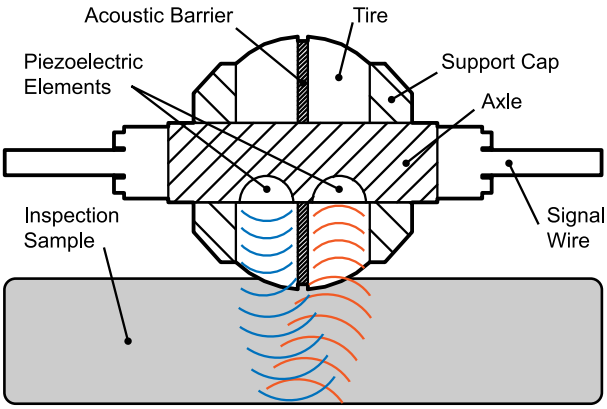

Fig. 4. A dual element wheel probe cross-sectional view and diagram of ultrasound wave propagation during measurement. The tire outer diameter is approximately 25 mm and its mass is 53 g including the connecting cables.

During inspection, deformation of the solid rubberized tire replicates the action of common liquid or gel couplants: displacing reflective or scattering acoustically discontinuous air pockets held at the tire-sample interface. However, dry coupling mechanisms are sensitive to surface roughness and fine particulate dust as these features retain air pockets. They represent a complex effect on operability: influenced by material conformability, applied force, feature size and distribution [49], [50].

In commercial applications of this wheel probe, thickness measurements have been successful against in situ painted steel assets with typical mean arithmetic surface roughness (R_a) well above 10 µm. Brushing of the tire surface with a thin layer of oil has also proven effective against dust particles [51]. Similar ability to measure through surface coatings to that of commercial thickness gages may be expected, typically up to 1 mm to 2.5 mm of paint [52], [53], provided the coating is non-scattering and well bonded to the substrate. Surface coatings failing to meet these criteria may require removal.

In practice, we find mechanical force circa 20 N acting through the wheel probe tire creates sufficient deformation to obtain a usable signal above the instrumentation noise floor. This force, akin to a firm single digit press by a human, is small but non-trivial if inspecting lightweight structures, such as airfoil skin or HVAC ducting. In these scenarios, prior assessment should confirm that the coupling load and any initial transient force can be safely supported.

Protrusion of the deformable tire beyond the flanking support caps is similarly found to permit acoustic coupling at probe angles within approximately ±10° of surface normal: an improvement over the ±3° alignment tolerance observed using hard-faced probes [39]. These pressure and orientation criteria therefore define the physical interaction necessary for this probe to support ultrasonic measurement.

2) Ultrasonic Signal Transceiver

The piezoelectric elements of the dry-coupling transducer are driven by a small form-factor transceiver, custom designed for mobile robotic applications [54]. Its functional components are depicted in Fig. 5. During operation, this instrumentation draws below 100 mA from the onboard 12 V power supply: a minimal detriment to UAV flight duration.

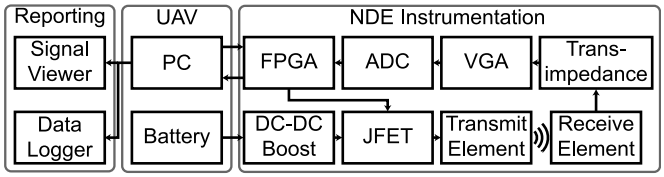

Fig. 5. Functional block diagram of the embedded dual channel ultrasonic transceiver. Instrumentation hardware fits within a 136 mm x 61 mm x 33 mm footprint and has a mass of 78 g excluding connecting cables.

The transceiver module contains two discrete channels: a transmission channel and a receiver channel, one for each piezoelectric element. Transmission uses a JFET transistor to briefly connect the transducer element to the DC-DC boosted supply voltage and produce a 180 V single pulse excitation at a repetition frequency of 100 Hz. Received signals pass through a discrete transimpedance amplifier and variable gain amplifier (VGA) then are digitized to 8 bits by the analog to digital converter (ADC) at a sampling rate of 100 MHz. Samples are buffered in FPGA memory before transfer to the UAV embedded computer (PC) via USB2.0. Available FPGA memory imposes maximum recorded signal length of 81.92 µs per transmission, sufficient to capture thickness measurements up to 25 cm in aluminum. Recorded signals are passed through a Butterworth bandpass filter with 60 dB attenuation outside ±2 MHz of the probe center frequency. This mitigates noise induced by the high-power switching of UAV flight systems and any other electromagnetic interference.

Captured signals are timestamped and published in real-time to the ROS network hosted by the UAV embedded PC. This enables live display of A-scan signals via Wi-Fi link to a ground based computer. Further, all ROS published ultrasound and UAV telemetry data is recorded. Numeric thickness inference and target relative measurement localization may thus be post-processed to generate a detailed inspection report, as below.

III. Experimental Assessment Methodology

A number of trials were conducted within an indoor laboratory flight volume to quantify performance of the integrated system. We provide details of this facility and the assessment strategy employed.

A. Flight Testing Facility

Experiments were conducted within a dedicated flight volume. This space included a flexible mounting frame: a repositionable planar wall upon which target inspection samples could be rigidly affixed. A similar structure allows for the positioning of test-pieces on the underside of an overhanging surface with adjustable inclination.

As the facility is indoors, the multirotor platform must operate in a GNSS denied environment, as is often the case in industrial settings. It may instead use localization provided by multiple Vicon motion capture cameras [43], giving full position and orientation measurement at 100 Hz.

Whereas the Voliro craft is similarly capable of environmental interaction when employing other localization technologies during outdoor operation, this setup is common to laboratory testing of aerial robotics. It provides accurate reference data for quantitative performance assessment and may be purposefully degraded to examine UAV controller function amid pose uncertainty.

The testing volume also includes a power tether, providing high voltage DC current to the UAV from a domestic supply via an onboard step-down converter. This is not necessary for flight but may be used in place of standard LiPo batteries for convenience.

B. Inspection Samples

Two samples were used in the analysis of the inspection capability of the dry-coupling over-actuated remote thickness measurement system. These are depicted in Fig. 6, with measurement details in TABLE I and TABLE II.

Thin plate and stepped bar geometries are chosen to be representative of defects arising from large scale corrosive material thickness loss in petrochemical storage tanks and similar inspection scenarios. Both are constructed of aluminum, highlighting capability for aerial contact interaction without relying upon magnetic adhesion.

Each sample is used to assess different aspects of system performance. The plate sample provides a large surface area over which the positional repeatability of interaction may be assessed. Additionally, the thinnest features enable performance characterization as the measured distance approaches the accepted practical limit of one ultrasonic wavelength in the material under test (less than 1.3 mm for a 5 MHz wave in aluminum) [47]. Concertedly, the bar sample is designed to assess the resolution of changing thickness during dynamic scanning of the wheel probe along a target surface. Geometry of the bar contains precision manufactured 1 mm stepped changes in thickness from 31.5 mm to 17.5 mm then further 0.1 mm steps down to a minimum thickness of 16.5 mm over a length of 500 mm at a step width of 20 mm.

Reference geometry of the samples is captured using calibrated micrometer calipers at regular intervals across the sample. Each sample is then reconstructed mathematically as a collection of planes, minimizing the total least squares distance from the measured points of to their fitted plane via singular value decomposition [55]. These objects may be interrogated to give sample thickness at all locations.

Sample reference thickness may then be determined by intersection of a line passing though the point of contact on the exposed front surface with the plane describing the sample rear wall, per the equations for line-plane intersection established in standard 3D geometry [56]. Direct numerical comparison between the ultrasonic measurements and manufactured geometry is thus enabled.

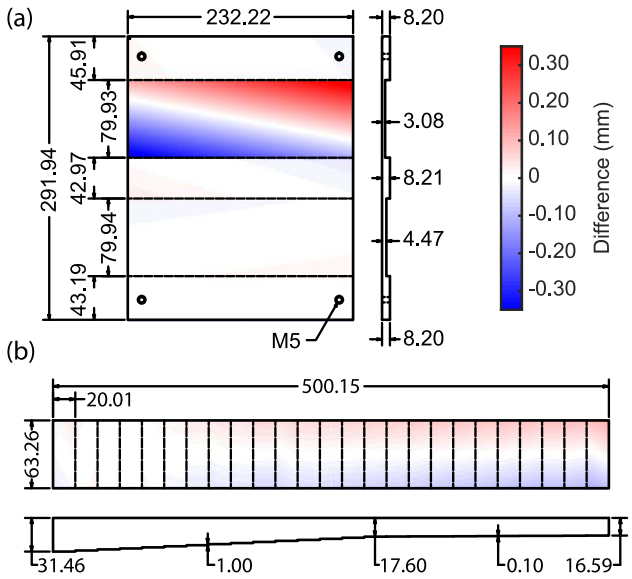

Fig. 6. As manufactured dimensions of aluminum plate sample, (a), and stepped bar sample, (b). All dimensions are in millimeters. Thickness dimensions are the mean within each region, with the difference from this value illustrated via the colormap. Step thickness changes are given in (b).

TABLE I PLATE SAMPLE THICKNESS AS MANUFACTURED

Region ID	Mean (mm)	± Max. Difference (mm)	Region ID	Mean (mm)	± Max. Difference (mm)
1	8.20	0.02	**4**	4.47	0.02
2	3.08	0.38	**5**	8.20	0.01
3	8.21	0.03			

Regions in Fig. 6(a) are numbered top to bottom.

TABLE II BAR SAMPLE THICKNESS AS MANUFACTURED

Region ID	Mean (mm)	± Max. Difference (mm)	Region ID	Mean (mm)	± Max. Difference (mm)
1	31.46	0.03	**14**	18.60	0.07
2	30.56	0.02	**15**	17.60	0.07
3	29.54	0.01	**16**	17.51	0.07
4	28.56	0.01	**17**	17.40	0.08
5	27.57	0.02	**18**	17.29	0.08
6	26.58	0.02	**19**	17.19	0.09
7	25.59	0.04	**20**	17.08	0.09
8	24.60	0.05	**21**	16.98	0.09
9	23.62	0.04	**22**	16.88	0.09
10	22.65	0.06	**23**	16.78	0.09
11	21.62	0.07	**24**	16.68	0.10
12	20.63	0.06	**25**	16.59	0.12
13	19.60	0.06			

Regions in Fig. 6(b) are numbered left to right.

Under this method finer features, such as shallow surface scrapes or other minor variations in surface texture, are not captured by the fitted planes. However, effects of any such features are negligible, owing to insensitivity of dual-element probes to surface roughness, advantageous when measuring corroded material [57]. Additionally, small scale surface warping or curvature is indistinguishable within the footprint of the transducer. The sample representation is therefore simplified to construct the front face as a single geometric plane, with the back-wall planes retaining their relative offset.

Reference thickness can then be directly determined as the height above the datum plane of the intersection between a line passing through the measurement point and the back-wall.

C. Ultrasonic Thickness Measurement

When assessing thickness ultrasonically, the geometry of the sample under test is inferred by directly measuring the time-of-flight (ToF), T, of the ultrasound pressure wave as it travels into the sample, reflects of the back-wall boundary and returns to the receiving transducer. The material thickness, d, is then found by using this time, the speed of sound in the material for the propagating wave-mode, v, and an integer factor, n, correcting for the number of traversals of the material thickness, calculated as:

$$d = \frac{vT}{n} \tag{6}$$

By convention a constant speed of sound is assumed, as obtained from a table of nominal values [58] or determined via calibration against a sample of the same material and of known dimensions, per the relevant inspection standard [47], [48]. In this "pulse-echo" configuration, n has the value 2 as T measures propagation of the ultrasonic wave-packet following reflection from a rear boundary then returning to the transducer on the front: a path through double the material thickness.

Thickness measurement accuracy thus depends on the confidence in the wave propagation speed and the ability to extract the time of flight from the recorded signal. Here, we discuss considerations specific to the dry-coupling dual-element wheel probe and its experimental usage.

Speed of sound for each sample is determined experimentally using a manual calibration procedure against known geometry under optimal dry-coupled conditions. Results presented in TABLE III are within the standard range for rolled aluminum accounting for small metallurgical variations [58].

TABLE III

SAMPLE ULTRASONIC WAVE VELOCITY CALIBRATION DATA

Sample	Number of Readings	Reference Thickness (mm)	Calculated Speed of Sound (m/s)	Standard Deviation (m/s)
Plate	2000	8.211	6416.767	13.956
Bar	2000	31.460	6404.814	4.1574

In measuring the time-of-flight to infer thickness, we note that thinning deformation of the dry-coupling transducer under pressure causes variation in the arrival time of the first echo from the tire-sample boundary, depicted at t_0 in Fig. 7.

A stronger interaction force between the UAV and inspection sample compresses the rubberized tire and shortens the return path length, also non-linearly increasing the signal amplitude, as illustrated. However, the time-of-flight between backwall echoes of index $i-1$ and i, denoted T_i, is independent of tire compression. We therefore determine time-of-flight via auto-correlation: a method insensitive to variation in t_0.

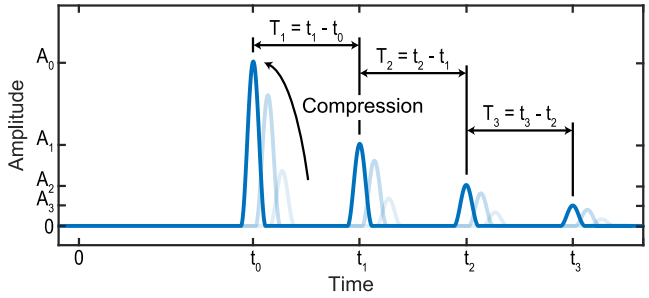

Fig. 7. A synthetic ultrasonic A-scan signal waveform showing the inter-echo time-of-flight, T_i. Increasing tire compression shortens the first echo transit time, t_0, and improves coupling, increasing signal amplitude. Inter-echo time is unaffected by compression.

Correlation based time-of-flight measurements are well established in literature [59], [60] and are noted for their performance in cases of low Signal to Noise Ratio (SNR). In some regards they are considered optimal, owing to their use of all information held in the signal [59].

Applying the auto-correlation function to an ultrasonic signal returns a waverform symmetrical about zero lag. The inter-echo period may then be determined from the first positive lag time at which the amplitude reaches a local maximum peak. This peak corresponds to the time-of-flight between subsequent echo signals granting the best alignment of all recorded reverberations across the sample, weighted by their relative amplitude. Such a method also permits measurement of material beneath ultrasonically transmissive exterior coatings, e.g. paint, owing to its basis in inter-echo time-of-flight and the small amplitude of coating-substrate bounday reflections relative to the backwall echoes.

However, a dual element probe will exhibit a small bias in the extracted time-of-flight due to the 'V' shaped propagation path, illustrated in Fig. 4. This effect arrises due to transmit and receive element separation and is most consequential where this distance forms a large component of the total propagation path length, typically in samples thinner than 3 mm [48]. By similar effect, time-of-flight will vary slightly between A-scan echoes, rising asymptotically towards the perpendicular transit time as the number of reverberations increases. This effect is proportionally translated to measured thickness by (6). Fig. 8 depicts measurement of the thinnest plate sample region most susceptable to V-path effects. Using the speed calibration data of TABLE III, ultrasonic readings of the region may be subject to a worst case undersizing thickness uncertainty of up to 0.12 mm versus the perpendicular transit.

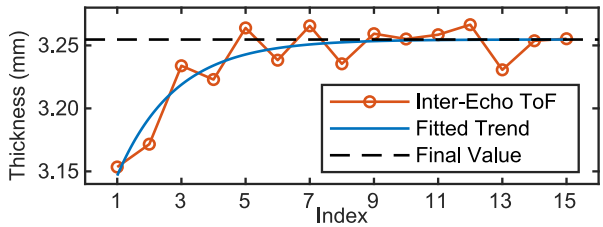

Fig. 8. The trend in measured thickness using the inter echo time-of-flight, T_i. This is captured in the thinnest region of the plate sample, where the V-path effect is most significant, under optimal dry-coupling conditions.

These effects are mitigated in practice by the presence of multiple distinct echoes, granting a reading closer to the perpendicular thickness. Other strategies such as empirical correction curve generation may reduce error across the range of thicknesses under test [48]. Any residual error will then form a component of the thickness measurement uncertainty in the system assessment of Section IV.

D. Sample-Relative Measurement Localization

To quantitatively profile system inspection performance, measurements taken while in contact with the sample must be identified and their results compared to reference geometry. Null measurements taken outside contact, or when contact has failed to meet the acoustic coupling criteria, are identified by a peak amplitude below a threshold level set approximately 12 dB above the instrumentation RMS noise floor.

Position of the valid ultrasound readings relative to the sample is derived from the UAV pose estimate provided by the flight volume Vicon motion capture system fused with the onboard Inertial Measurement Unit (IMU) data. A similar process may be applied to improve data rate and reduce uncertainty when operating under other positioning technologies. Here, using the timestamps of both the ultrasound and UAV pose messages provided by a consistent computer clock, the full 6 DoF pose of the craft in the world frame at the instant of thickness measurement is determined by linear interpolation of its position and interpolation of its quaternion orientation via the Spherical Linear intERPolation (SLERP) method [61]. In contrast to purely linear quaternion interpolation, SLERP assumes a constant angular velocity between orientations. Movement during the 82 µs where the ultrasonic signal is captured is deemed negligible at the recorded flight speeds.

The line along which measurements may be acquired accounting for variable compression of the wheel probe tire is then defined in the UAV body frame by a unit vector parallel to the probe arm and intersecting the frame origin, situated at its center of mass. (Note that the axis of the end effector passes through the center of mass as a feature of the Voliro design, minimizing the turning moment of interaction forces.) Expression of this measurement line in the world frame using the interpolated UAV pose permits the point of inspection to be determined by solution of the line-plane intersection equations [56] using the plane of the exposed sample face.

Registration of the sample is performed to empirically define this plane within the world frame. The positions of multiple known points on the sample are measured using the Vicon system and used to produce a homogeneous transformation matrix via a least-squares rigid point cloud fitting algorithm [62]. The inverse of this transform then maps the world frame location of each ultrasound reading to the sample coordinate frame wherein the sample reference geometry may be queried for thickness at that location. Thickness error statistics are then obtained by comparison with the ultrasonically measured value.

IV. Results

A number of experiments are conducted to demonstrate and assess the integrated ultrasonic inspection system[1]. Whereas UAV flight telemetry and ultrasonic signals may be remotely viewed in real-time, the more detailed target relative localization and thickness reference comparison analyses are generated by post-processing of recorded data.

A. Vertical Wall Thickness Measurement

First, a simple interaction with the vertically mounted aluminum plate, as in Fig. 9, is considered with the UAV manually piloted to engage at three points of different thickness. Between point measurements surface contact is disengaged. The craft is then moved to the next point and the probe aligned to the surface before contact is re-entered for measurement. From take-off to landing, this process was completed in under 48 s.

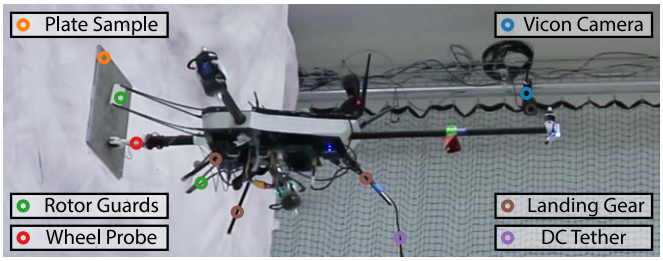

Fig. 9. The UAV positions and applies the probe to the plate sample face, meeting the coupling pressure and orientation requirements to record thickness measurements. Rotor guards protecting against accidental surface collision are attached to the UAV body during testing. Power is supplied by the DC tether for convenience.

Remaining in contact for a minimum period of 2 s at each point, the 100 Hz pulse repetition frequency allows capture of multiple thickness measurements. For illustrative purposes, a single ultrasonic echo signal or "A-scan" from each measurement location is presented in Fig. 10. The characteristic echo signal is clearly visible indicating orientation during contact is maintained within the probe alignment tolerance of ±10° relative to surface normal and coupling force circa 20 N is exerted, sufficient to permit full acoustic coupling.

Considering all readings at each point, Fig. 11 gives the mean measured numerical thicknesses, their standard deviations and plots error versus reference geometry across the trial flight. Times at which the probe was in contact supporting measurement are highlighted using the timestamps of recorded A-scan signals. The error quantization bands are a consequence of the sampling period of the NDE instrumentation ADC and the propagation speed of the longitudinal ultrasonic wave. Given a sampling period of 10 ns and speed of approximately 6400 m/s, (6) dictates a minimum thickness resolution of just above 0.032 mm, as is visible here.

By analysis of the measurement data illustrated in Fig. 11, we provide a quantitative profile of system measurement accuracy in this scenario via the statistical data of TABLE IV. Therein, mean absolute error (MAE) describes system

[1] We include a supplementary multimedia video file showing these assessments, also available at https://bit.ly/3qCsrFT .

precision, indicating the distribution of successful measurements relative to the reference thickness. Mean Error (ME) indicates overall system accuracy, averaging data from multiple readings to mitigate random effects and evaluate any systemic error. Typical lower and upper error boundaries of the any single reading are indicated by the 5th and 95th percentile metrics, respectively.

TABLE IV WALL THICKNESS MEASUREMENT ERROR STATISTICS

Number of Readings	Mean Absolute Error (mm)	5th Percentile Error (mm)	Mean Error (mm)	95th Percentile Error (mm)
766	0.0766	-0.1766	0.0112	0.1068

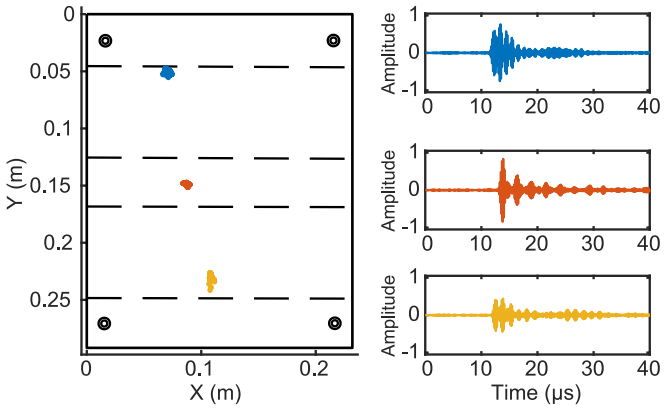

Fig. 10. A map of the points on the sample outer face inspected during the test flight. Recorded ultrasonic echoes from each point to the correspond to the locations indicated opposite. Signals are normalized relative to the maximum amplitude recorded in the trial.

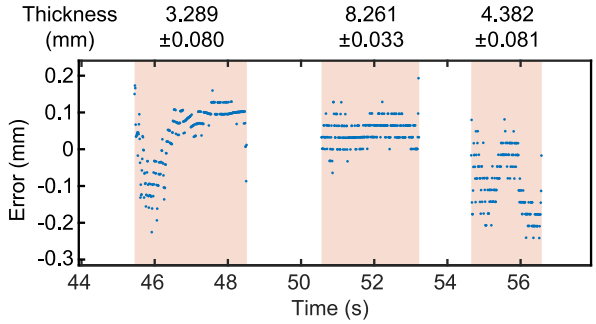

Fig. 11. Error in the remote measurement versus reference geometry plotted across the time of the flight trial. Numerical annotations give mean thickness measurements and standard deviation. Highlights demarcate times of surface contact supporting measurement.

MAE below 0.1 mm indicates a level of system performance comparable to some commercially available hand-held ultrasonic thickness gauges with similar pricing [52], [63], [64]. Additionally, system ME magnitude is less than the 0.032 mm minimum single measurement resolution for this instrumentation. ME is superior to thin sample measurements reported in literature using commercial, UAV-targeted, instrumentation, which showed consistent errors of 0.6 mm across multiple readings [36]. An asymmetrical error distribution is described by the 5th and 95th percentile errors, demonstrating a slight bias towards undersized thickness measurements, which may be attributed to residual V-path effects. However, the overall measurement accuracy shown in the positive mean error indicates that undersized measurements, though larger in magnitude, are less frequent. The observed error statistics therefore make an encouraging comment on measurement accuracy and repeatability given the relative infancy of contact based aerial inspection.

B. Point Inspection Repeatability

In this experiment to profile system capability for repeated stable measurement interaction, the integrated UAV system is manually piloted through multiple interactions with the plate sample, targeting the marked target position. The locations of these measurements are presented in Fig. 12.

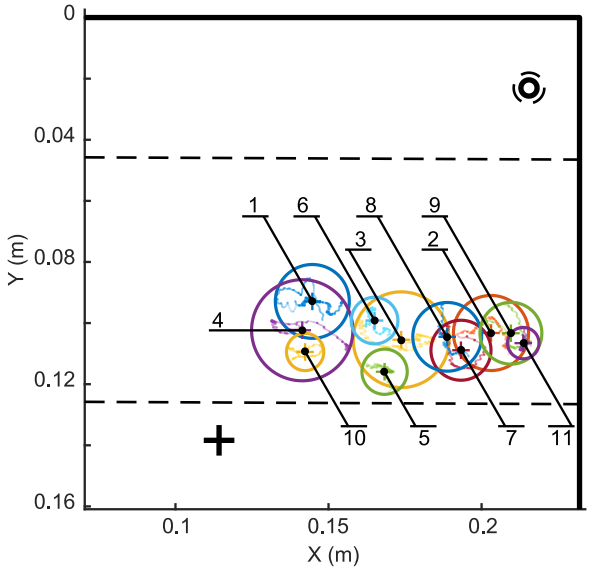

Fig. 12. Map of inspection points acquired through repeated interaction with upper right quadrant of target plate sample showing position uncertainty boundary. The targeted point on the plate is marked '+'. Point labels indicate the sequence of acquisition.

Position encoding of the measured thicknesses relative to the sample is projected from the UAV pose per Section III.D and so exhibits uncertainty related to both the translation and rotation estimates. This uncertainty will vary depending on the positioning technology used. In attempting to correct position error versus an estimate with excessive noise, the controller response may knock the UAV out of contact with the target surface. However, fusion with onboard inertial data mitigates global position noise effects and grants the stable relative pose estimate necessary for NDE interactions under a range of indoor and outdoor positioning technologies.

An indication of the system measurement localization accuracy under laboratory conditions is provided visually in Fig. 12 and numerically in TABLE V. These uncertainty radii quantify the worst-case distance from the mean location of each contact instance to the furthest single projected location captured in the same interaction.

From the data of TABLE V it is clear that the UAV is able to make stable contact in a repeatable manner, satisfying the probe 20 N and ±10° coupling conditions in all interactions. These 11

measurements were completed in a period of under 143 s with minimal pilot intervention other than to approach and retreat from the sample surface. The system successfully captured data during each interaction; all maintained for at least 2 s.

TABLE V MEASUREMENT REPEATABILITY DATA

Point Index	Number of Samples	Distance to Mean Center (X, Y) (mm)		Distance to Target (mm)	Position Uncertainty Radius (mm)	SNR (dB)	Thickness MAE (mm)
1	653	-32.01	-11.80	54.74	12.08	29.79	0.106
2	323	26.37	-1.46	95.54	12.29	39.39	0.111
3	385	-2.97	0.74	68.01	15.67	35.32	0.142
4	320	-35.31	-2.36	45.13	16.55	39.40	0.036
5	323	-8.41	11.22	58.55	7.40	39.53	0.079
6	393	-11.68	-5.53	64.17	7.63	39.96	0.155
7	308	16.55	4.18	84.35	9.81	36.63	0.073
8	260	12.05	-0.21	81.87	11.24	38.92	0.072
9	351	32.86	-1.39	101.58	10.11	31.58	0.148
10	242	-34.36	4.75	40.34	6.09	33.02	0.091
11	204	36.90	1.86	104.35	5.14	38.86	0.029

Calculating the SNR of an A-scan as the ratio of its overall maximum amplitude to the local maximum amplitude of the received signal before the first ultrasonic echo, all such interactions grant mean SNR near 30 dB and above. Over all readings in this trail the system demonstrated thickness MAE of 0.095 mm, comparable to the previous experiment.

Considering precision of the transducer positioning, the mean location of each labeled contact point is within a maximum distance from the average across all points of 37 mm and 12 mm in the sample x and y axes, respectively. Over all trial contact point locations, the average distance to the target point is 73 mm, quantifying positioning accuracy. This accuracy, however, is expected to vary between repeated trials owing to the tolerance requested from the pilot, time taken to execute the motion, and other human factors, such as skill level and viewpoint.

C. Accessing the Underside of Overhanging Structures

Utilizing the ability of the Voliro aerial manipulator platform to actively re-orient its thrust relative to its body, a stable hover can be maintained in a number of pitch orientations. Further, it remains possible to exert force and perform environmental interaction in such poses, as in Fig. 13. This enables application to numerous inspection scenarios concerning both vertical surfaces and the underside of overhanging structures. Following alignment of the UAV to the overhanging surface normal, its pose during repeated measurement acquisition is given in Fig. 14. Therein, times of inspection are marked using the timestamps of captured A-scans with peak amplitude level higher than approximately 12 dB above the RMS noise floor and so indicative of successful deployment. Again, the probe criteria for full acoustic coupling of orientation within ±10° of surface normal and 20 N interaction force are satisfied.

As before, a plot of the measured thickness error versus the reference sample geometry is provided in Fig. 15 with statistical data describing the distribution of error magnitude given in TABLE VI.

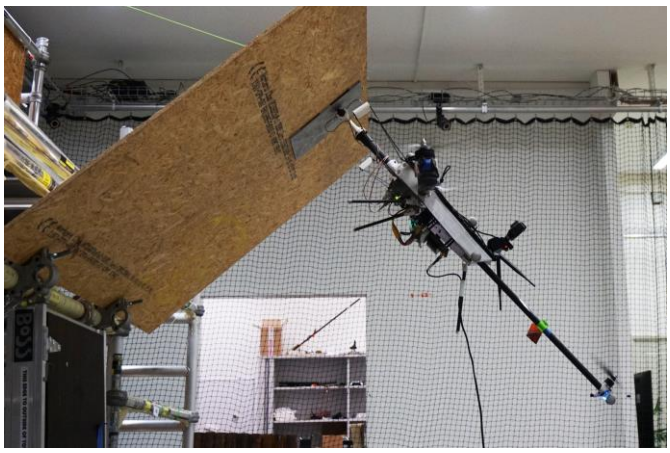

Fig. 13. The Voliro manipulator platform is able to enter and maintain stable contact with the underside of an overhanging surface. The inclination of the overhang is approximately 45°. Supports on the hidden side of the surface provide its rigidity, acting against force exerted by the UAV.

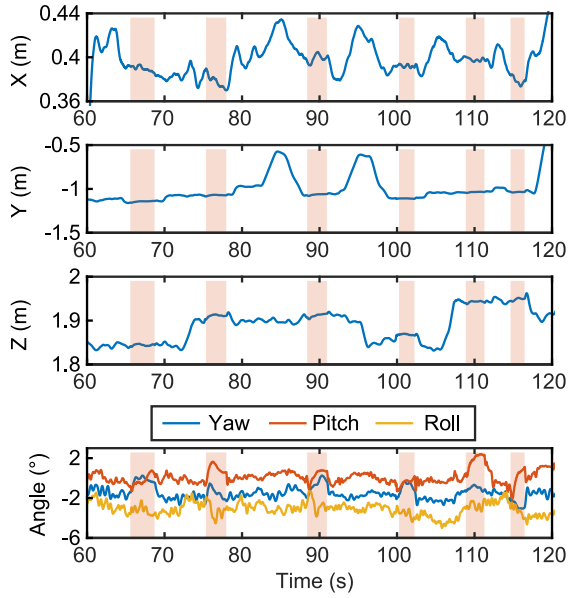

Fig. 14. The UAV flightpath when inspecting the underside of an overhanging structure. Times where surface contact supported ultrasonic measurement are highlighted. Yaw, pitch and roll Euler angles relative to the ideal surface normal inspection pose are plotted under Z-Y-X convention.

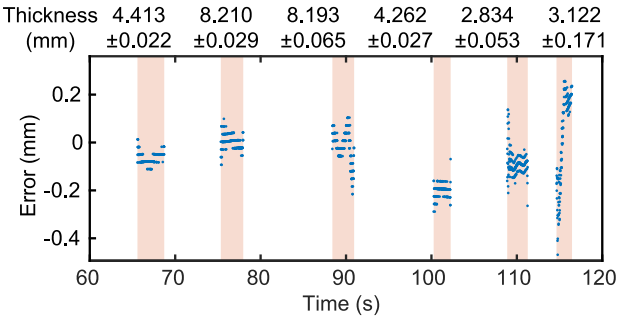

Fig. 15. Error plot of thickness measurements from the underside of an overhanging surface versus reference geometry. Annotations give numerical thickness measurements and their standard deviation. Highlights demarcate times of contact measurements.

TABLE VI TILTED MEASUREMENT ACCURACY STATISTICS

Number of Readings	Mean Absolute Error (mm)	5th Percentile Error (mm)	Mean Error (mm)	95th Percentile Error (mm)
1482	0.0924	-0.2249	-0.0536	0.1600

The MAE of the ultrasound measurements versus reference geometry is comparable to previous results, indicating the performance is retained while operating in non-standard orientations on the underside of target structures. As before, the 5th and 95th percentile distribution points describe an asymmetrical distribution, favoring larger magnitude under-sizing errors. Overall measurement uncertainty has increased with the change in attitude, but remains within usable limits.

This demonstrable and quantified capability to perform multi-orientation point thickness measurement with consistent accuracy and precision represents a significant development in the context of existing aerial ultrasonic NDE systems supporting measurement interaction in only one orientation [35], [37], or providing no quantitative discussion of measurement accuracy [29].

D. Dynamic Scanning Measurement Acquisition

A final trial is conducted as an assessment of system performance when capturing a stream of measurements, rolling along the sample surface. As such, extended area thickness maps may be constructed from a series of scanned lines. This modality offers enhanced time efficiency and data density versus conducting serial discrete point measurements. We assess the capability to capture thickness features with a lateral spacing of 20 mm. Flight trajectory is set by the pilot while the flight controller maintains interaction force and orientation. Fig. 16 provides a still image captured during this process.

From Fig. 17 the capability to acquire measurements via scanning may be observed. Combining the data of two contiguous passes along the sample length, remaining gaps are smaller than the scale of reportable features for this trial. The largest single region without coverage spanned a distance of 10.9 mm. It occurred near the leftmost point of Fig. 17(a) as the scanning motion was halted and its direction changed before the return pass.

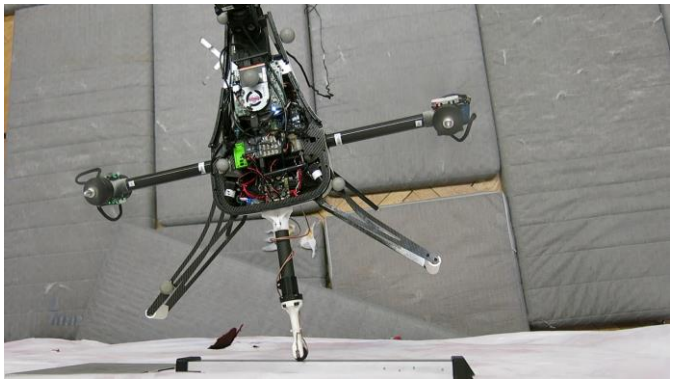

Fig. 16. A top-down view of the UAV scanning across the stepped aluminum bar. This was captured during the second of two passes completed within a continuous contact interaction; traversing from left to right to left as pictured.

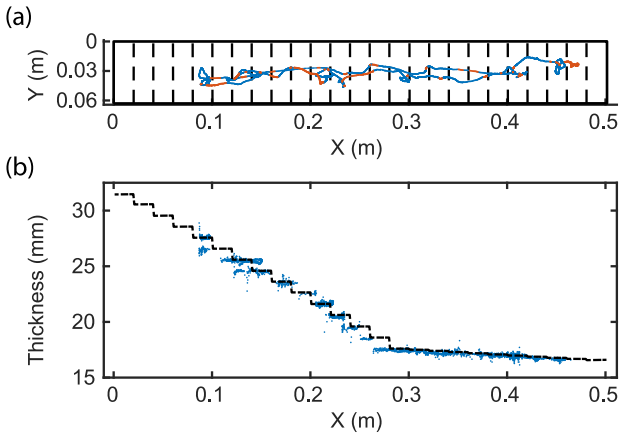

Fig. 17. Aerial thickness measurement scans of the bar sample along its x-axis. (a) Points of inspection projected to the sample surface. Successful measurements are blue. Null or unsuccessful measurements are orange. (b) Position encoded bar thickness profile measurements. Each reading is a single blue point. The dashed line gives cross-sectional reference geometry.

The full scan path across the sample was completed in under 65 s, traveling a total distance of 0.71 m. Using the horizontal location of each measurement on the sample, as projected from the recorded UAV pose estimate per the method of Section III.D, we plot numerical thickness versus position in Fig. 17(b), describing the sample cross-section. All thickness step features within the scanned region are captured in the depicted data. In the plot left and center 1 mm step thickness changes are readily distinguishable. However, the smaller 0.1 mm steps are close to measurement accuracy limits established above so are challenging to discern. As above, error statistics are given in TABLE VII. These indicate some loss of accuracy during the dynamic process, as may be expected.

TABLE VII SCANNING MEASUREMENT ACCURACY STATISTICS

Number of Readings	Mean Absolute Error (mm)	5th Percentile Error (mm)	Mean Error (mm)	95th Percentile Error (mm)
5197	0.2788	-1.0553	-0.1416	0.7389

These effects are attributed in part to measurement position uncertainty. Visible as horizontal shift of some features in Fig. 17(b), sample relative localization uncertainty of the magnitude given in TABLE V can see measurements wrongly assigned to neighboring step features in the reference geometry. This is visible directly in the approach of the 5th and 95th percentile errors to the 1 mm step thickness change of the bar sample. However, within an industrial context, position uncertainty at this scale will only influence sizing and localization of smaller features. It will have little impact on overall detectability or localization of larger scale flat pitting, or uniform and mesa-type corrosion features.

Through this contiguous scanning process, measurements were acquired with a success rate of 86.44 %. A recorded signal with peak amplitude falling below the 12 dB RMS noise-relative threshold for usable readings is considered a failed measurement. Here failure occurs where contact exists, as observable in the included video file, but falls short of the 20 N

force and ±10° from surface normal requirements for full acoustic coupling. This effect may also degrade SNR to marginally above the usability threshold and so cause the small number of outlier measurements visible in Fig. 17(b).

The times at which coupling was successful are visible in the highlight overlay of Fig. 18, plotting the world frame UAV flightpath. For optimal inspection performance the UAV should maintain the probe arm orientation along the sample surface normal with the direction in which the wheel-probe rolls parallel to the length of the sample.

Fig. 18 also plots the angular error between this ideal pose and the craft orientation decomposed to Z-Y-X convention Euler angles as before. Examination indicates that ineffectual measurements are common to sudden position changes or large angular offsets from surface normal, i.e. where pressure and orientation fall outside probe coupling limits. These effects are due to the nature of the tire rolling resistance during dynamic motion and transition from the static case.

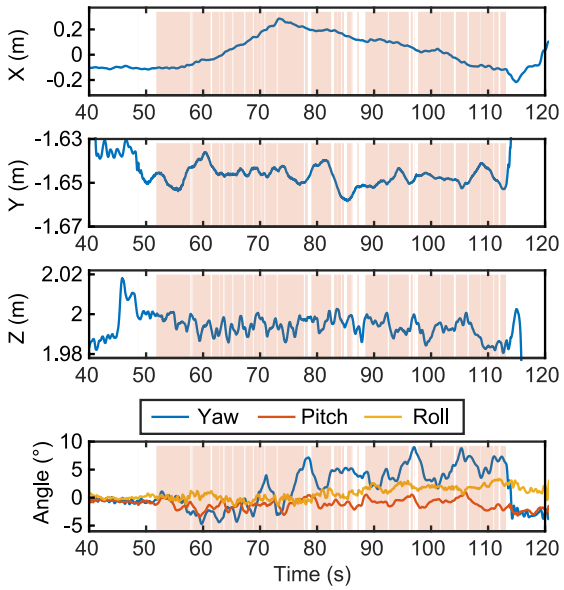

Fig. 18. The UAV flightpath while conducting a rolling scan measurement. Highlighted regions denote times when usable signals were acquired. Euler angle orientation is given relative to the ideal surface normal inspection pose.

While meeting the probe coupling force and orientation requirements, the UAV must also counteract a significant static friction force component parallel to the target surface to commence rolling. As before, compressive force acting through the tire couples it to the piezoelectric elements in the axle, allowing ultrasonic transmission. However, additional coupling force also increases friction about the axle owing to the design of the probe, introducing further complexity. Once motion starts static friction is quickly replaced by a weaker dynamic component. Consequently, the wheel presents a reduced resistance to motion and accelerates rapidly upon mode transition. Inertia of the UAV prevents its matching of this motion, instead arresting the wheel after a short distance. Repeated switching between these friction modes forms an irregular motion that has low average speed along the target surface but is sufficient to support NDE measurement activity.

V. Discussion

In consideration of the overall system we draw comparison to the state-of-the-art in the from of TABLE VIII assessing capability relative to those recent works listed in Section I.A demonstrating aerial ultrasonic NDE.

TABLE VIII SYSTEM COMPARISON WITH STATE OF THE ART

Ref.	Herein	[29]	[35]	[37]	[38]	[39]
Rotor Layout	Tri	Octo	Quad	Quad +2	Quad	Quad
Actuation	Over	Over	Under	Under	Under	Under
Interaction[a]	VT	MT	RU	DP	RU	RU
Accessible Surfaces	Omni	Omni	Floor, Pipe	Wall	Ceiling	Wall
Effector[b]	Rod R	Arm A	Grip R	Frame C	Rod C	Rod C
Probe Elements	Dual, Wheel	Dual	EMAT	Single	Single	Dual
Couplant[c]	Dry	Gel D	EM	Gel D	Gel M	Gel M
NDE Type	Point, Scan	Point, Scan	Point	Point	Point	Point

Key: [a] UAV interaction force generation method i.e. *VT:* Vectored Thrust, *MT:* Multidirectional Thrust, *DP*: Dedicated Propellers, *RU:* Reoriented unidirectional body thrust.
[b] UAV effector structure type i.e. *A*: Actuated, *C*: Complaint, *R*: Rigid.
[c] Couplant mechanism i.e. *D*: Automatically dispensed gel, *M*: Manually applied gel, *EM*: Electromagnetic induction.

All works listed in TABLE VIII conduct static, point thickness ultrasonic measurements. However, many are limited in applicability to single orientation interaction modes: contacting vertically planar walls [37], [39], the underside of horizontally planar ceilings [38], or depositing a sensor package atop horizontal plates and pipes [35]. We show increased applicability to the generic in situ inspection process through the multidirectional target interactions of Section IV by development of a novel thrust vectoring, bi-axial tilting propeller, over-actuated tricopter architecture.

Comparatively, under-actuated quadrotors with unidirectional thrust, [35], [38], [39], exhibit strong coupling between attitude and translational dynamics. To control interaction forces they must reorientate the full UAV body, potentially incurring ultrasonic probe motion and degrading its measurements. Here, and in [29], over-actuation decouples attitude and translation, enabling force omnidirectionality. Generation of net thrust in all directions about the body grants full interaction control with direct stabilization by the main flight systems while the UAV holds static pose. As such, requirements are relaxed for mechanical stabilization structures such as interaction specific single DoF complaint effectors [37]–[39], or additional dedicated propellers, as in [37] where two horizontal axis propellers generate interaction thrust but are unused in free flight. There is also no reliance on NDE transducer specific forces such as in [35] where the attraction of the EMAT package, held by a rigid gripper beneath the UAV, aids gravity to stabilize deployment against magnetic targets.

Further, over-actuation by dynamic vectoring of the propellers, as used here, removes both the counteracting internal wrench components found when using the net effect

from multidirectional thrust superposition [29], and the resultant penalty to energy efficiency. A greater proportion of the total thrust is thereby available outside of the vertical direction, enabling pose omnidirectionality in stable flight with adjustable non-horizontal attitude. Where [29] makes omnidirectional contact with the target from a consistent horizontal pose using a 6 DoF actuated arm that rotates about the center of mass, the system herein may directly align its body to the surface normal direction. Contact inspection is then reliably performed with a simple rigid effector, as in Section IV.B and Section IV.C, reducing system size and complexity while increasing ability for efficient remote inspection within crowded industrial airspace.

Direct quantitative comparison of ultrasonic measurement performance is limited by a lack of common procedures and metrics among existing publications. Of the works in TABLE VIII, only [37], [38] and [39] quantify inspection measurement accuracy versus a known dimensioned target. Against a vertical aluminum plate with thickness ranging from 9 mm to 15 mm, [39] reports a mean absolute error of 0.12 mm, whereas [37] shows consistent error of -0.6 mm versus a 6 mm thick plate of unspecified metal, attributed to sensor calibration. Performance validation in [38] reports an error of +0.46 mm, but the slower speed of sound in the 5 mm thick, horizontally mounted, acrylic sample limits comparability. Capability for both point thickness and scanning measurement is indicated in [29], but the authors present no quantitative ultrasonic data for comparison.

Addressing this, we present a full characterization of ultrasonic thickness measurement accuracy versus known dimensioned aluminum samples in a well-defined procedure. Data obtained in repeated static point and rolling scan measurements of vertical aluminum samples using a dry-coupling ultrasonic wheel probe, show mean absolute error below 0.1 mm and 0.3 mm respectively. Whereas previous systems have required the manual application of ultrasonic couplant gel in an additional preparatory step [38], [39], or instead carry an onboard gel reservoir and dispensation mechanism [29], [37], we present a new mode of aerial ultrasonic inspection, improving process efficiency and aiding utilization where couplant gel may be contaminative. This inspection modality is compatible with electrically non-conductive targets, increasing applicability over EMAT solutions [35]. Additionally, we present an application-focused quantification of both the repeat interaction positioning accuracy versus a target point and the propagation of combined uncertainty from UAV position and attitude estimates to the inferred, sample relative, measurement location. Such aspects are critical during extended timescale asset monitoring. Results in Section IV thus provide practical benchmarks evincing the utility of this technology for in situ NDE process automation.

VI. Future Works

We identify a number of research goals that may further develop integrated system utility within an industrial context.

Additional investigation of the dynamic scanning process is expected to yield strategies for mitigation of its discontinuous friction effects. Sensor based feedback of interaction force and surface relative probe odometry into an application specific control algorithm would allow a smoother rolling motion while guaranteeing satisfaction of the probe coupling criteria. This would increase scanning speed and coverage reliability, also improving measurement position registration and minimizing redundant passes for area thickness mapping.

Development and integration of an algorithmic correction for V-path uncertainty would increase thin-wall measurement confidence, similarly improving practical utility.

Quantitative study of measurement accuracy in consideration of disturbance effects caused by outdoor specific positioning technologies and weather systems including near-structure airflow, surface dust particles or precipitation may provide strong evidence of the systems commercial utility.

Lastly, algorithms for inspection flightpath planning around complex industrial asset geometry optimally utilizing the over-actuated capability are suggested to grant full automation and efficiency improvements of the aerial inspection process.

VII. Conclusions

Building on currently published works pertaining to remote aerial inspection, operating principles for an aerial inspection platform integrating an over-actuated UAV with a 5 MHz dry-coupling ultrasonic wheel probe to perform contact based volumetric inspection are presented.

An application focused assessment of system capability shows that the UAV is readily capable of point interaction with the test samples, meeting and maintaining the probe coupling and pressure requirements. Empirical trials demonstrate successful measurement acquisition in numerous orientations.

In point thickness measurements taken of vertical surfaces and on the underside of overhanging structures, mean absolute error below 0.1 mm is observed when compared to the sample reference dimensions. This indicates a level of performance comparable to some hand-held commercial thickness measurement equipment.

Lastly, we assess utilization of the wheel probe for continuous thickness mapping along a linear path. This demonstrated the recording of the cross-sectional dimensions of a precision manufactured aluminum test piece. Stepped changes in thickness of 1 mm spaced at 20 mm increments along the sample length are clearly visible in the processed inspection data, despite small gaps in coverage of under 11 mm where the dynamics of the rolling motion cause a temporary loss of coupling. Future work is proposed to further enhance this capability, directly addressing these challenges.

Ultimately, the UAV aerial inspection system is found to be successful in its application of ultrasonic NDE and is presented with quantified, application contextualized, uncertainty bounds. This represents a means of improving the inspection process efficiency and operator safety in hazardous conditions common to industrial environments.

References

[1] The American Society for Nondestructive Testing, “Codes and Standards Overview,” 2019.

https://www.asnt.org/MajorSiteSections/Standards.aspx (accessed Jan. 31, 2020).

[2] UK Health and Safety Executive, "Inspection/Non Destructive Testing: Regulatroy Requirements." https://www.hse.gov.uk/comah/sragtech/techmeasndt.htm#RegulatoryRequirements (accessed Jan. 16, 2020).

[3] P. Horrocks, D. Mansfield, K. Parker, J. Thomson, T. Atkinson, and J. Worsley, "Managing Ageing Plant: A Summary Guide." http://www.hse.gov.uk/research/rrpdf/rr823-summary-guide.pdf (accessed Oct. 31, 2019).

[4] N. Meyendorf *et al.*, "NDE 4.0—NDE for the 21st Century—The Internet of Things and Cyber Physical Systems will Revolutionize NDE," *Cent. Nondestruct. Eval. Conf. Pap. Posters Present.*, Jan. 2017, [Online]. Available: https://lib.dr.iastate.edu/cnde_conf/117

[5] UK Health and Safety Executive, "Human factors/ergonomics, health and safety in the workplace." http://www.hse.gov.uk/humanfactors/index.htm (accessed Oct. 31, 2019).

[6] X. Li, Q. Yang, Z. Chen, X. Luo, and W. Yan, "Visible defects detection based on UAV-based inspection in large-scale photovoltaic systems," *IET Renew. Power Gener.*, vol. 11, no. 10, pp. 1234–1244, 2017, doi: 10.1049/iet-rpg.2017.0001.

[7] O. Menéndez, M. Pérez, and F. Auat Cheein, "Visual-Based Positioning of Aerial Maintenance Platforms on Overhead Transmission Lines," *Appl. Sci.*, vol. 9, no. 1, p. 165, Jan. 2019, doi: 10.3390/app9010165.

[8] L. Wang, Z. Zhang, and X. Luo, "A Two-Stage Data-Driven Approach for Image-Based Wind Turbine Blade Crack Inspections," *IEEEASME Trans. Mechatron.*, vol. 24, no. 3, pp. 1271–1281, Jun. 2019, doi: 10.1109/TMECH.2019.2908233.

[9] J. Seo, L. Duque, and J. Wacker, "Drone-enabled bridge inspection methodology and application," *Autom. Constr.*, vol. 94, pp. 112–126, Oct. 2018, doi: 10.1016/j.autcon.2018.06.006.

[10] P. Rossi, F. Mancini, M. Dubbini, F. Mazzone, and A. Capra, "Combining nadir and oblique UAV imagery to reconstruct quarry topography: methodology and feasibility analysis," *Eur. J. Remote Sens.*, vol. 50, no. 1, pp. 211–221, Jan. 2017, doi: 10.1080/22797254.2017.1313097.

[11] A. Khaloo, D. Lattanzi, K. Cunningham, R. Dell'Andrea, and M. Riley, "Unmanned aerial vehicle inspection of the Placer River Trail Bridge through image-based 3D modelling," *Struct. Infrastruct. Eng.*, vol. 14, no. 1, pp. 124–136, Jan. 2018, doi: 10.1080/15732479.2017.1330891.

[12] S. Agnisarman, S. Lopes, K. Chalil Madathil, K. Piratla, and A. Gramopadhye, "A survey of automation-enabled human-in-the-loop systems for infrastructure visual inspection," *Autom. Constr.*, vol. 97, pp. 52–76, Jan. 2019, doi: 10.1016/j.autcon.2018.10.019.

[13] Ida, Nathan and Meyendorf, Norbert, *Handbook of modern non-destructive testing*. Switzerland: Springer Nature, 2017. [Online]. Available: https://doi.org/10.1007/978-3-319-26553-7

[14] G. Splitt, "New Applications for Dry Coupling Probes," in *Non-Destructive Testing*, London, UK, Sep. 1987, pp. 2300–2304. doi: 10.1016/B978-0-08-036221-2.50015-2.

[15] J. M. Allin, P. Cawley, and M. J. S. Lowe, "Adhesive disbond detection of automotive components using first mode ultrasonic resonance," *NDT E Int.*, vol. 36, no. 7, pp. 503–514, Oct. 2003, doi: 10.1016/S0963-8695(03)00045-8.

[16] C. Mineo *et al.*, "Robotic Geometric and Volumetric Inspection of High Value and Large Scale Aircraft Wings," in *2019 IEEE 5th International Workshop on Metrology for AeroSpace (MetroAeroSpace)*, Torino, Italy, Jun. 2019, pp. 82–86. doi: 10.1109/MetroAeroSpace.2019.8869667.

[17] B. Drinkwater and P. Cawley, "An Ultrasonic Wheel Probe Alternative to Liquid Coupling," in *Review of Progress in Quantitative Nondestructive Evaluation*, D. O. Thompson and D. E. Chimenti, Eds. Boston, MA: Springer US, 1995, pp. 983–989. doi: 10.1007/978-1-4615-1987-4_124.

[18] C. F. Britton, "4.36 Corrosion Monitoring and Inspection," in *Shreir's Corrosion*, vol. 4, Bob Cottis, Michael Graham, Robert Lindsay, Stuart Lyon, Tony Richardson, David Scantlebury, and Howard Stott, Eds. Elsevier, 2010, pp. 3117–3166. Accessed: Dec. 08, 2020. [Online]. Available: https://doi.org/10.1016/B978-044452787-5.00130-X

[19] Y. Abdulla and Y. Narasimha, "Successful inspection of two large ammonia storage tanks," *Process Saf. Prog.*, vol. 28, no. 1, pp. 45–59, 2009, doi: 10.1002/prs.10278.

[20] V. Kain, "Flow Accelerated Corrosion: Forms, Mechanisms and Case Studies," *Procedia Eng.*, vol. 86, pp. 576–588, Jan. 2014, doi: 10.1016/j.proeng.2014.11.083.

[21] J. Harfield, "Client guide for the inspection of steel chimneys," Association of Technical Lightning & Access Specialists (ATLAS), London, UK, ASG 003, Dec. 2018. Accessed: May 14, 2020. [Online]. Available: https://atlas.org.uk/?mdocs-file=1364

[22] L. T. Popoola, A. S. Grema, G. K. Latinwo, B. Gutti, and A. S. Balogun, "Corrosion problems during oil and gas production and its mitigation," *Int. J. Ind. Chem.*, vol. 4, no. 1, p. 35, Sep. 2013, doi: 10.1186/2228-5547-4-35.

[23] L. R. Hilbert, A. R. Black, F. Andersen, and T. Mathiesen, "Inspection and monitoring of corrosion inside monopile foundations for offshore wind turbines," Stockholm, Sweden, Sep. 2011, p. 14.

[24] "UAV Integrated UT," *TexoDrone*. http://www.texodroneservices.co.uk/service/uav_integrated_ut (accessed May 15, 2019).

[25] "RoNik Inspectioneering - Engineering Robotic inspections." http://www.inspectioneering.eu/ (accessed May 30, 2019).

[26] "Ultrasonic Inspection UAV," *Air Control Entech*. https://aircontrolentech.com/ (accessed May 15, 2019).

[27] R. Voyles and G. Jiang, "Hexrotor UAV platform enabling dextrous interaction with structures — Preliminary work," in *2012 IEEE International Symposium on Safety, Security, and Rescue Robotics (SSRR)*, Nov. 2012, pp. 1–7. doi: 10.1109/SSRR.2012.6523891.

[28] M. Ryll, H. H. Bülthoff, and P. R. Giordano, "A Novel Overactuated Quadrotor Unmanned Aerial Vehicle: Modeling, Control, and Experimental Validation," *IEEE Trans. Control Syst. Technol.*, vol. 23, no. 2, pp. 540–556, Mar. 2015, doi: 10.1109/TCST.2014.2330999.

[29] M. Á. Trujillo, J. R. Martínez-de Dios, C. Martín, A. Viguria, and A. Ollero, "Novel Aerial Manipulator for Accurate and Robust Industrial NDT Contact Inspection: A New Tool for the Oil and Gas Inspection Industry," *Sensors*, vol. 19, no. 6, Mar. 2019, doi: 10.3390/s19061305.

[30] M. Tognon *et al.*, "A Truly-Redundant Aerial Manipulator System With Application to Push-and-Slide Inspection in Industrial Plants," *IEEE Robot. Autom. Lett.*, vol. 4, no. 2, pp. 1846–1851, Apr. 2019, doi: 10.1109/LRA.2019.2895880.

[31] P. J. Sanchez-Cuevas *et al.*, "Fully-Actuated Aerial Manipulator for Infrastructure Contact Inspection: Design, Modeling, Localization, and Control," *Sensors*, vol. 20, no. 17, p. 4708, Aug. 2020, doi: 10.3390/s20174708.

[32] M. Kamel *et al.*, "The Voliro Omniorientational Hexacopter: An Agile and Maneuverable Tiltable-Rotor Aerial Vehicle," *IEEE Robot. Autom. Mag.*, vol. 25, no. 4, pp. 34–44, Dec. 2018, doi: 10.1109/MRA.2018.2866758.

[33] K. Bodie *et al.*, "An Omnidirectional Aerial Manipulation Platform for Contact-Based Inspection," Freiburg im Breisgau, Germany, Jun. 2019, vol. 15. Accessed: Oct. 07, 2019. [Online]. Available: http://www.roboticsproceedings.org/rss15/p19.html

[34] K. Bodie *et al.*, "Active Interaction Force Control for Contact-Based Inspection With a Fully Actuated Aerial Vehicle," *IEEE Trans. Robot.*, pp. 1–14, 2020, doi: 10.1109/TRO.2020.3036623.

[35] R. Jarvis, A. Farinha, M. Kovac, and F. Cegla, "NDE sensor delivery using unmanned aerial vehicles," *Insight - Non-Destr. Test. Cond. Monit.*, vol. 60, no. 8, pp. 463–467, Aug. 2018, doi: 10.1784/insi.2018.60.8.463.

[36] L. M. González-deSantos, J. Martínez-Sánchez, H. González-Jorge, M. Ribeiro, J. B. de Sousa, and P. Arias, "Payload for Contact Inspection Tasks with UAV Systems," *Sensors*, vol. 19, no. 17, p. 3752, Jan. 2019, doi: 10.3390/s19173752.

[37] L. M. González-deSantos, J. Martínez-Sánchez, H. González-Jorge, F. Navarro-Medina, and P. Arias, "UAV payload with collision mitigation for contact inspection," *Autom. Constr.*, vol. 115, p. 103200, Mar. 2020, doi: 10.1016/j.autcon.2020.103200.

[38] B. B. Kocer, T. Tjahjowidodo, M. Pratama, and G. G. L. Seet, "Inspection-while-flying: An autonomous contact-based nondestructive test using UAV-tools," *Autom. Constr.*, vol. 106, p. 102895, Oct. 2019, doi: 10.1016/j.autcon.2019.102895.

[39] D. Zhang, R. Watson, C. MacLeod, G. Dobie, W. Galbraith, and G. Pierce, "Implementation and evaluation of an autonomous airborne ultrasound inspection system," *Nondestruct. Test. Eval.*, vol. 0, no. 0, pp. 1–21, Feb. 2021, doi: 10.1080/10589759.2021.1889546.
[40] T. Ikeda *et al.*, "Wall contact by octo-rotor UAV with one DoF manipulator for bridge inspection," in *2017 IEEE/RSJ International Conference on Intelligent Robots and Systems (IROS)*, Sep. 2017, pp. 5122–5127. doi: 10.1109/IROS.2017.8206398.
[41] S. Hamaza *et al.*, "Sensor Installation and Retrieval Operations Using an Unmanned Aerial Manipulator," *IEEE Robot. Autom. Lett.*, vol. 4, no. 3, pp. 2793–2800, Jul. 2019, doi: 10.1109/LRA.2019.2918448.
[42] F. Ruggiero, V. Lippiello, and A. Ollero, "Aerial Manipulation: A Literature Review," *IEEE Robot. Autom. Lett.*, vol. 3, no. 3, pp. 1957–1964, Jul. 2018, doi: 10.1109/LRA.2018.2808541.
[43] Vicon Motion Systems Ltd, "Vicon Applications: Engineering." https://www.vicon.com/applications/engineering/ (accessed Mar. 12, 2020).
[44] "Total Stations | Leica Geosystems." https://leica-geosystems.com/en-GB/products/total-stations (accessed Nov. 01, 2019).
[45] D. Scaramuzza and Z. Zhang, "Aerial Robots, Visual-Inertial Odometry of," in *Encyclopedia of Robotics*, M. H. Ang, O. Khatib, and B. Siciliano, Eds. Berlin, Heidelberg: Springer, 2020, pp. 1–9. doi: 10.1007/978-3-642-41610-1_71-1.
[46] "Home | Eddyfi." https://www.eddyfi.com (accessed Oct. 09, 2020).
[47] Technical Committee ISO/TC 135, "ISO 16809:2017 Non-destructive testing – Ultrasonic thickness measurement," International Standards Organisation, Geneva, Switzerland, International Standard ISO 16809:2017, Nov. 2017. Accessed: Nov. 01, 2019. [Online]. Available: https://www.iso.org/standard/72430.html
[48] E07 Committee, "E797: Standard Practice for Measuring Thickness by Manual Ultrasonic Pulse-Echo Contact Method," ASTM International, Dec. 2015. doi: 10.1520/E0797_E0797M-15.
[49] B. Drinkwater, R. Dwyer-Joyce, and P. Cawley, "A study of the transmission of ultrasound across solid–rubber interfaces," *J. Acoust. Soc. Am.*, vol. 101, no. 2, pp. 970–981, 1997, doi: 10.1121/1.418055.
[50] D. Benstock, F. Cegla, and M. Stone, "The influence of surface roughness on ultrasonic thickness measurements," *J. Acoust. Soc. Am.*, vol. 136, no. 6, pp. 3028–3039, Dec. 2014, doi: 10.1121/1.4900565.
[51] G. Dobie, R. Summan, C. MacLeod, G. Pierce, and W. Galbraith, "An automated miniature robotic vehicle inspection system," in *40th Annual Review of Progress in Quantitative Non-Destructive Evaluation*, Baltimore, Maryland, USA, 2014, pp. 1881–1888. doi: 10.1063/1.4865053.
[52] Cygnus instruments, "Cygnus 2+ Hands-Free." Accessed: Dec. 02, 2020. [Online]. Available: https://www.cygnusinstruments.co.uk/product/cygnus-2-hands-free-2/
[53] Waygate Technologies, "DM5E corrosion thickness gauges," *Baker Hughes Digital Solutions*. https://www.bakerhughesds.com/ndt-ultrasonic-testing/thickness-gauges/dm5e-corrosion-thickness-gauges (accessed Dec. 01, 2020).
[54] C. N. Macleod, G. Dobie, S. G. Pierce, R. Summan, and M. Morozov, "Machining-Based Coverage Path Planning for Automated Structural Inspection," *IEEE Trans. Autom. Sci. Eng.*, vol. 15, no. 1, pp. 202–213, Jan. 2018, doi: 10.1109/TASE.2016.2601880.
[55] G. E. Farin and D. Hansford, *Mathematical principles for scientific computing and visualization*. Wellesley, Mass: AK Peters, 2008.
[56] E. W. Weisstein, "Line-Plane Intersection," *Mathworld-- A Wolfram Web Resource*. http://mathworld.wolfram.com/Line-PlaneIntersection.html (accessed Oct. 24, 2019).
[57] Olympus, "Corrosion Gaging with Dual Element Transducers." https://www.olympus-ims.com/en/applications/corrosion-gaging-dual-element-transducers/ (accessed Jan. 04, 2020).
[58] Dwight E. Gray, *American Institue of Physics Handbook*, 3rd ed. New York, NY, USA: McGraw-Hill, 1972.
[59] M. Parrilla, J. J. Anaya, and C. Fritsch, "Digital signal processing techniques for high accuracy ultrasonic range measurements," *IEEE Trans. Instrum. Meas.*, vol. 40, no. 4, pp. 759–763, Aug. 1991, doi: 10.1109/19.85348.
[60] D. Marioli, C. Narduzzi, C. Offelli, D. Petri, E. Sardini, and A. Taroni, "Digital time-of-flight measurement for ultrasonic sensors," *IEEE Trans. Instrum. Meas.*, vol. 41, no. 1, pp. 93–97, Feb. 1992, doi: 10.1109/19.126639.
[61] K. Shoemake, "Animating Rotation with Quaternion Curves," in *Proceedings of the 12th Annual Conference on Computer Graphics and Interactive Techniques*, New York, NY, USA, 1985, pp. 245–254. doi: 10.1145/325334.325242.
[62] K. S. Arun, T. S. Huang, and S. D. Blostein, "Least-Squares Fitting of Two 3-D Point Sets," *IEEE Trans. Pattern Anal. Mach. Intell.*, vol. PAMI-9, no. 5, pp. 698–700, Sep. 1987, doi: 10.1109/TPAMI.1987.4767965.
[63] "27MG Ultrasonic Thickness Gage." https://www.olympus-ims.com/en/27mg/#!cms[tab]=%2F27mg%2Fspecifications (accessed Jun. 29, 2020).
[64] "Multigauge 5600 Hand Held Ultrasonic Thickness Meter | Tritex NDT," *Tritex NDT Ltd*. https://www.tritexndt.com/product/mg5600-ultrasonic-thickness-meter (accessed Nov. 04, 2019).

Robert Watson is a PhD candidate within the department of electrical & electronic engineering at the University of Strathclyde, Glasgow, UK. He attained an MEng degree in electrical and mechanical engineering at Strathclyde in 2017, with first class honors, including a year of international study at the University of Toronto, Canada.

His current research interests in robotics and automation as applied to remote, in-situ, non-destructive evaluation of industrial assets, including wind and nuclear energy generation infrastructure. These objectives are supported by industrial partners in the UK Research Centre of EDF Energy and the National Nuclear Laboratory.

Mina Kamel received his PhD at the Autonomous Systems Lab of ETH Zurich. During his PhD, he focused on control and design of aerial manipulation systems. During this engagement, he led and supervised several projects. After his PhD, he co-founded Voliro AG, an ETH Zurich spin-off developing advanced omnidirectional aerial robots for physical work at height. In 2019 he was selected among 100 Digital Shapers in Switzerland by Bilanz business magazine.

Dayi Zhang (S'15-M'20) is a Research Associate in the Department of Electronic and Electrical Engineering at the University of Strathclyde. He received a PhD degree in autonomous unmanned aerial vehicles for non-destructive testing. His current research interests are in the field of in-situ ultrasonic and photogrammetry inspections.

Gordon Dobie is a Senior Lecturer in Electronic & Electrical Engineering at the University of Strathclyde, UK. He has 15 years' experience and about 70 publications in automation, structural inspection, sensors and signal processing. Dr Dobie has a strong track record in industrial engagement working with partners in the Oil and Gas, Nuclear and Healthcare sectors to deliver novel solutions to real industrial problems. His work led directly to an onsite robotic inspection of a critical path reprocessing vessel at Sellafield. Dr Dobie has licensed key parts of his team's mobile robotics technology to SME members of the Research Centre for Non-Destructive Evaluation. He currently leads a team of 20 PhD/EngD students and postdoctoral researchers.

Charles MacLeod is a Chancellor's Fellow and Senior Lecturer in the Centre for Ultrasonic Engineering. After being awarded a Masters in Electrical and Mechanical Engineering with Distinction at Strathclyde, Charles then went on to undertake a PhD in Automated Non–Destructive Evaluation.

His research is primarily associated with the inspection and manufacturing enhancement of high value assets and components. He leads a number of high-profile inter-disciplinary inspection research projects. While undertaking his PhD, Charles was seconded to Spirit AeroSystems, in Prestwick to undertake Knowledge Exchange activities built on fundamental EPSRC funded research. Charles was awarded an EPSRC Doctoral Prize for 2014, for his work investigating automated non-contact ultrasound.

Juan Nieto (S'02-M'06) received his PhD in field robotics at the University of Sydney. Afterwards, he worked at the Rio Tinto Centre for Mine Automation, leading the perception and mapping team. He is currently Deputy Director at the Autonomous Systems Lab at ETH. His main research focus in on perception and navigation for mobile robots. He has published over 200 manuscripts in international conferences and journals.

S. Gareth Pierce holds the Spirit AeroSystems/ Royal Academy of Engineering Research Chair for In-Process Non-Destructive Testing of Composites, and leads a multidisciplinary team at Strathclyde University.

He is a board member for the UK Research Centre in NDE, promotes collaborative research through an international network of academic partners and promotes impact though relationships with multi sector industry partners and the UK High Value Manufacturing Catapult Centres. Based in the Centre for Ultrasonic Engineering, the focus of his work is robotics and autonomous systems for inspection, including non-destructive testing and evaluation (NDT&E) for manufacture, and structural health monitoring (SHM) for asset inspection. The multidisciplinary nature of his work brings together robotics, instrumentation and interfacing, applied optics, ultrasonics, 3D metrology and machine learning based data management. These themes resonate closely with the fundamental concepts of Industry 4.0.